

## 1 Background and Motivation

A rocket engine operates by ejecting stored mass to generate thrust, capitalizing on the conservation of momentum described by Newton's third law. Chemical rockets are commonly used in space launch vehicles where vehicle mass optimization is crucial to overall performance, with solid, hybrid, and liquid propellant variants. The importance of mass optimization can be seen by performing a simple analysis on the velocity increment ( $\Delta v$ ) imparted by a rocket operating at constant thrust over its duration. Assuming the vehicle starts from rest, the velocity increment is given by equation 1, where  $m_0$  is the initial mass,  $m_f$  is the final mass, and  $c$  is the effective exhaust velocity, defined by  $F = \dot{m}c$  where  $F$  is the rocket thrust and  $\dot{m}$  is the propellant mass flow rate.

$$\Delta v = c \ln(m_0/m_f) = c \ln\left(\frac{m_p + m_s}{m_s}\right) \quad (1)$$

In this expression  $m_p$  is the propellant mass and  $m_s$  is the mass of the structure and we have ignored any payload mass. From this it can be clearly seen that to maximize the velocity increment, the fraction needs to be as large as possible which occurs when the structural mass is the smallest. This is especially important given the high cost of access to space. Previously it has cost upwards of \$10,000/kg to put material in orbit. Private space flight companies are working to lower this barrier to entry but prices are still on the order of thousands of dollars per kilogram.

Of interest here is the design of a regeneratively cooled liquid bipropellant rocket engine thrust chamber, nozzle, and cooling jacket which will be optimized to minimize structural mass given thrust/efficiency requirements and material structural and thermal limitations for liquid methane-oxygen propellants. In a regeneratively cooled engine a portion of one of the propellants is split from the main feed line and routed through a cooling jacket surrounding the entire thrust chamber. After passing through the cooling jacket the coolant is recombined with the main propellant feed and brought into the combustion chamber. In most cases the fuel is used as the cooling fluid and that is the case here. The cooling jackets typically have a counter-flow arrangement with the main chamber discharge, meaning the coolant enters the jacket at the nozzle exit plane and leaves at the top near the combustion chamber. The design and analysis of rocket engines is highly multidisciplinary, drawing from fluid mechanics, thermodynamics, chemical kinetics, heat transfer, and solid mechanics to name a few. Thus it is a prime problem for multidisciplinary analysis and optimization. Simple models for many of these processes are developed and combined to drive said optimization.

## 2 Problem Statement and Design Parameters

In words, the problem statement is to minimize the structural mass  $m_s$  of a regeneratively cooled thrust chamber subject to thrust ( $F$ ), efficiency ( $I_{sp}$ ), mechanical stress ( $\sigma$ ), and operating temperature ( $T$ ) inequality constraints given a cryogenic propellant combination. The structural mass includes the combustion chamber and nozzle side walls and cooling jacket - the injector face is not part of the considered structural mass. The problem is stated explicitly in Equation 2, where the propellant combination and materials of construction are fixed.

$$\begin{aligned} &\text{minimize} && m_s(x) \\ &\text{s.t.} && F_{min} - F(x) \leq 0 \\ &&& I_{sp,min} - I(x) \leq 0 \\ &&& \|\sigma(x)\|_\infty - \sigma_{yield} \leq 0 \\ &&& \|T(x)\|_\infty - T_{max} \leq 0 \\ &\text{given :} && Y = \{\{\text{MaterialProperties}\}, \{\text{AmbientConditions}\}, \{\text{PropellantCombination}\}\} \end{aligned} \quad (2)$$

The problem is defined by the design variables listed in Table 1.

Table 1: Design Variables

| Design Parameter | Description                                       | Units  |
|------------------|---|--------|
| $r_c$            | Combustion chamber internal radius                | $m$    |
| $L_c$            | Combustion chamber length                         | $m$    |
| $\beta_{nc}$     | Nozzle converging section cone frustum half angle | deg.   |
| $\beta_{nd}$     | Nozzle diverging section cone frustum half angle  | deg.   |
| $\epsilon$       | Nozzle area ratio, $A_e/A_t$                      | -      |
| $t_w$            | Internal structure wall thickness                 | $m$    |
| $t_j$            | Cooling jacket channel thickness                  | $m$    |
| $t_s$            | Outer shell thickness                             | $m$    |
| $\dot{m}_f$      | Fuel mass flow rate                               | $kg/s$ |
| $\phi$           | Equivalence ratio                                 | -      |
| $p_c$            | Combustion chamber pressure                       | atm    |
| $f_c$            | Coolant fraction                                  | -      |

### 3 Models and Analysis

All of the models and analysis presented here were developed from scratch for this project. A few textbooks were instrumental in developing said models. In particular, [Sutton and Biblarz, 2010], [Huzel and Huang, 1992] and [Anderson, 2003] were referenced to develop the flow model and performance calculations. [Incropera et al., 2003] and [Sutton and Biblarz, 2010] were referenced to develop the thermal and mechanical stress models.

#### 3.1 Geometry Specification

The geometry of the combustion chamber and nozzle is simplified and parameterized with the internal volume treated as a body of revolution divided into three sections: combustion chamber, converging nozzle section, and diverging nozzle section. All sections are surrounded by the cooling jacket channel and outer shell. A schematic of an engine cross section is shown in Figure 1, where quantities in parentheses are computed from other design parameters. Analysis is carried out in cylindrical coordinates with the  $z$  axis aligned with the engine axis, about which axisymmetry in all models and analysis is assumed. Positive  $z$  is defined in the direction of propellant flow and is measured from the inside of the injector face at the top of the combustion chamber.

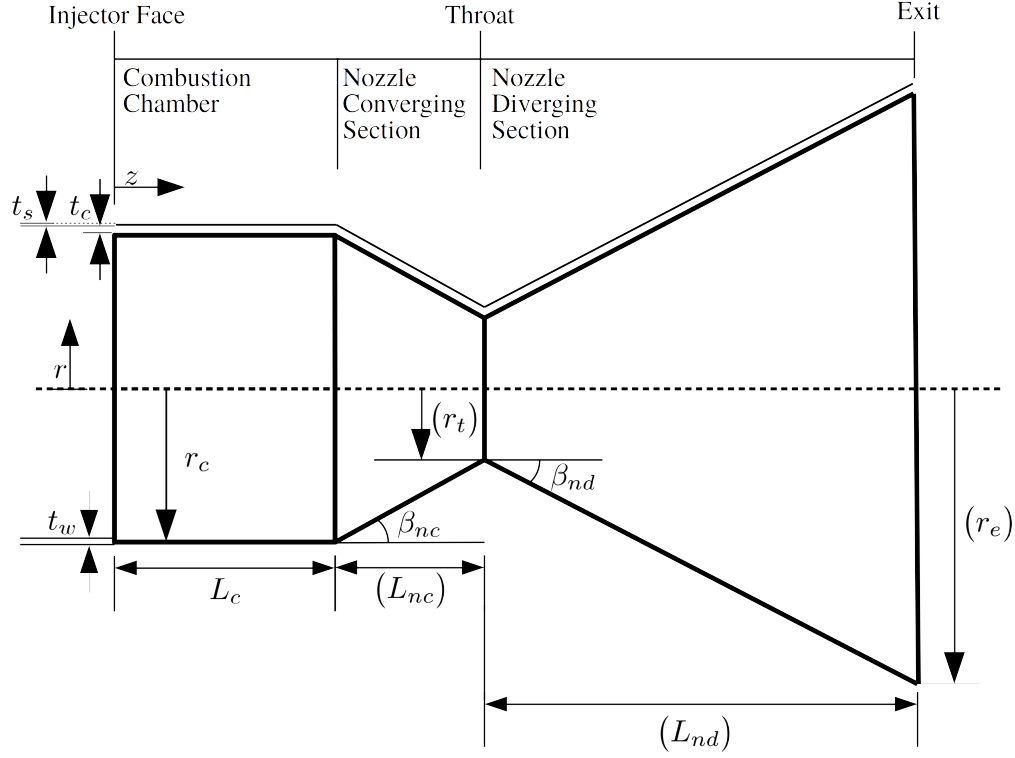


Figure 1: Simplified trust chamber geometry and design parameters. Quantities in parentheses  $(\cdot)$  are computed from the set of design parameters.

The flow through the nozzle is assumed to be quasi-1D and choked. Thus the continuity equation simplifies to  $\dot{m}_{tot} = \rho(z)A(z)u(z)$  which applies at any axial location  $z$  in the engine. Isentropic flow is assumed and standard relations may be used to write the mass flow rate through the engine throat as shown in Equation 3, where  $\gamma = c_p/c_v$  is the ratio of specific heats,  $R$  is specific gas constant defined as  $R = R_u/W$ , where  $R_u = 8.314 \text{ J}/(\text{mol} \cdot \text{K})$  is the universal gas constant. Additionally  $W$  is the gas molecular weight which is computed in the thermochemical model in addition to  $T_c$ . This is inverted to solve for the throat area  $A_t$  and thus the throat radius  $r_t$  as shown in Equation 4. This ensures the choked flow assumption is valid and is preferred over including  $r_t$  in the set of design parameters.

$$\dot{m}_{tot} = \rho_t A_t u_t = A_t p_c \gamma \frac{\sqrt{[2/(\gamma + 1)]^{(\gamma+1)/(\gamma-1)}}}{\sqrt{\gamma R T_c}} \quad (3)$$

$$A_t = \frac{\dot{m}_{tot} \sqrt{\gamma R T_c}}{p_c \gamma \sqrt{[2/(\gamma + 1)]^{(\gamma+1)/(\gamma-1)}}} \quad (4)$$

The nozzle exit area  $A_e$  and radius  $r_e$  then follow directly from design parameter nozzle area ratio ( $\epsilon$ ) as shown in Equation 5.

$$\epsilon = \frac{A_e}{A_t} \rightarrow A_e = \epsilon A_t \quad (5)$$

From this, the converging and diverging nozzle lengths  $L_{nc}/L_{nd}$  are computed readily from the cone half angles as shown in Equations 6 and 7.

$$L_{nc} = \frac{r_c - r_t}{\tan(\beta_{nc})} \quad (6)$$

$$L_{nd} = \frac{r_e - r_t}{\tan(\beta_{nd})} \quad (7)$$

Thus the specification of the geometry is not independent of the thermochemical properties of the propellant combination.

### 3.2 Mass Model

The total mass of the engine structure  $m_s$  is computed as shown in Equation 8.

$$m_s = m_c + m_{nc} + m_{nd} \quad (8)$$

The combustion chamber is modeled as a cylindrical shell, with the mass being computed readily from Equation 9.

$$\begin{aligned} m_c &= \rho_s L_c \pi [(r_c + t_w)^2 - r_c^2] \\ &= \rho_s L_c \pi [2r_c t_w + t_w^2] \end{aligned} \quad (9)$$

The converging and diverging nozzle sections are modeled as cone frustum shells. The volume of a cone frustum shell with  $r_2 > r_1$  and thickness  $t_w$  is computed as shown in Equation 10.

$$\begin{aligned} V &= \frac{\pi L}{3} [(r_1 + t_w)^2 + (r_2 + t_w)^2 + (r_1 + t_w)(r_2 + t_w) - r_1^2 - r_2^2 - r_1 r_2] \\ &= \frac{\pi(r_2 - r_1)t_w}{\tan(\beta)} [r_1 + r_2 + t_w] \end{aligned} \quad (10)$$

The second form of the expression results from the fact that  $\tan(\beta) = \frac{(r_2 - r_1)}{L}$ , where  $\beta$  is the cone frustum half angle. From this, the mass of the nozzle converging and diverging sections may be computed as shown in Equations 11 and 12.

$$m_{nc} = \frac{\rho_s \pi (r_c - r_t) t_w}{\tan(\beta_{nc})} [r_c + r_t + t_w] \quad (11)$$

$$m_{nd} = \frac{\rho_s \pi (r_e - r_t) t_w}{\tan(\beta_{nd})} [r_e + r_t + t_w] \quad (12)$$

The mass of the shell is not included in this calculation.  $t_s$  is still included in the set of design variables as this quantity has an effect on the heat transfer properties and therefore on the stresses in the internal wall.

### 3.3 Thermochemical Model

Cantera is used to compute the post combustion state given the combustion chamber pressure  $p_c$  and equivalence ratio  $\phi$ . The gri30 methane-air mechanism is used, although only a subset of the mechanism is required since the engine operates using liquid oxygen as the oxidizer instead of air. The balanced methane-oxygen combustion reaction is shown in Equation 13.



This equation is used to define the stoichiometric fuel-oxidizer mass ratio shown in Equation 14, where  $n_i$  is the number of moles of species  $i$  in the balanced equation and  $W_i$  is the corresponding molecular weight.

$$(F/O)_{st} = \frac{m_f}{m_o} = \frac{n_f W_f}{n_o W_o} \quad (14)$$

The equivalence ratio  $\phi$ , defined in Equation 15, and this mass ratio may be used to compute the oxidizer and thus total mass flow rate as shown in Equations 16 and 17.  $\phi < 1$  corresponds to fuel-lean conditions,  $\phi > 1$  corresponds to fuel-rich conditions, and of course  $\phi = 1$  corresponds to stoichiometric conditions.

$$\phi = \frac{(F/O)}{(F/O)_{st}} = \frac{\dot{m}_f / \dot{m}_o}{(F/O)_{st}} \quad (15)$$

$$\dot{m}_o = \frac{\dot{m}_f}{\phi(F/O)_{st}} \quad (16)$$

$$\dot{m}_{tot} = \dot{m}_f + \dot{m}_o \quad (17)$$

### 3.4 Flow Model

The fluid model used is based on the ideal rocket equations, presented in some form in both [Sutton and Biblarz, 2010] and [Huzel and Huang, 1992]. This model assumes quasi-1D compressible isentropic flow through the engine. The isentropic assumption is not strictly valid here since we are accounting for heat transfer from the working fluid to the rocket engine structure later in the thermal model. In reality the flow model and heat transfer model are coupled. However, the coupling is weak, where typically <1% of the thermal energy present in the working fluid after combustion is transferred to the walls. The ideal rocket model relies on simple, well established isentropic relations to compute the local properties relative to either the stagnation conditions or nozzle throat conditions.

#### 3.4.1 Combustion Chamber

The combustion chamber has constant cross sectional area along its length. Since heat transfer to the walls is ignored in the flow model, the fluid state is the same at all axial locations in the combustion chamber. A frozen flow assumption is used, where the composition of the gas is not allowed to change (it remains 'frozen') after combustion. Alternate models utilize shifting-equilibrium, where the composition of the gas is allowed to equilibrate up to the nozzle throat. The frozen flow assumption leads to under-prediction of rocket performance by about 1-4%, while shifting equilibrium is known to slightly over-predict engine performance. The gas velocity is computed from the continuity equation as shown in Equation 18.

$$\dot{m} = \rho_c A_c u_c \rightarrow u_c = \frac{\dot{m}}{\rho_c A_c} \quad (18)$$

The speed of sound is computed in the usual way as  $a_c = \sqrt{\gamma R T_c}$  and the Mach number is computed from its definition as  $M_c = u_c/a_c$ . The stagnation conditions are computed from the chamber properties using isentropic relations, listed generally in Equations 19-21, by setting station  $z$  to chamber conditions.

$$\frac{T_0}{T_z} = 1 + \frac{(\gamma - 1)M_z^2}{2} \quad (19)$$

$$\frac{p_0}{p_z} = \left[ 1 + \frac{(\gamma - 1)M_z^2}{2} \right]^{\gamma/(\gamma-1)} \quad (20)$$

$$\frac{\rho_0}{\rho_z} = \left[ 1 + \frac{(\gamma - 1)M_z^2}{2} \right]^{1/(\gamma-1)} \quad (21)$$

#### 3.4.2 Nozzle

The gas properties at each axial location in the nozzle are found by first solving the Mach Number-Area relation and then using isentropic relations. The Mach number area relation is as shown in Equation 22 and is valid between any axial locations 1 and 2 inside the engine.

$$\frac{A_1}{A_2} = \frac{M_2}{M_1} \sqrt{\left[ \frac{1 + [(\gamma-1)/2]M_1^2}{1 + [(\gamma-1)/2]M_2^2} \right]^{(\gamma+1)/(\gamma-1)}} \quad (22)$$

In this setting, the area ratio  $A_1/A_2$  is known along with either  $M_1$  or  $M_2$ . The expression is then used to solve for the other unknown Mach number. For convenience, we let station 2 be the nozzle throat, where the Mach number is known to be 1 due to the choked flow assumption (which is known to be valid due to the way the throat area is computed). Plugging in, squaring both sides, replacing subscript 1 with  $z$  to denote any axial location in the engine, and pulling both terms to one side of the expression (residual form) leads to Equation 23.

$$r(M_z) = \left( \frac{A_z}{A_t} \right)^2 - \frac{1}{M_z^2} \left[ \frac{1 + [(\gamma-1)/2]M_z^2}{1 + [(\gamma-1)/2]} \right]^{(\gamma+1)/(\gamma-1)} = 0 \quad (23)$$

This equation has two solutions for  $M_z$ , corresponding to subsonic and supersonic conditions. In the converging section of the nozzle the subsonic solution is selected, while in the nozzle the supersonic solution is chosen. The solutions are found using Newton's method for finding roots, where the derivative  $\partial r(M_z)/\partial M_z$

is taken analytically (not shown). Function `scipy.optimize.root_scalar()` is used for the implementation. The appropriate branch (subsonic/supersonic) is selected by specifying an initial guess equal to the upstream Mach number in the converging section, and an initial guess of  $M_z = 2$  in the diverging portion. With the Mach number on hand, isentropic relations in Equations 19-21 are inverted to solve for properties at station  $z$ . The flow model starts at the combustion chamber and works its way downstream. This is not necessary but improves the model convergence rate due to re-use of the previous solution as the starting guess.

### 3.4.3 Cooling Channel Flow

The coolant mass flow rate is specified by the coolant fraction which ranges from 0-1 as shown in Equation 24.

$$\dot{m}_{f,cool} = f_c \dot{m}_f \quad (24)$$

The pressure within the coolant channel at each axial location (denoted by superscript  $(i)$ ) is computed by setting the coolant channel outlet pressure to be  $1.5p_c$  and successively applying the hydraulic pipe equation shown in Equation 25 [Sutton and Biblarz, 2010].

$$p^{(i)} = p^{(i-1)} + \frac{1}{2} f \rho [u^{(i)}]^2 (L^{(i)} / D^{(i)}) \quad (25)$$

In the combustion chamber  $L = \Delta z_c$ , while in the nozzle  $L = \Delta z_n / \cos(\beta_n)$ , using the appropriate mesh spacing and half angle for converging and diverging sections.  $D = 4A/P$  is the hydraulic diameter where  $A$  is the cross sectional area and  $P$  is the wetted perimeter. The cooling jacket is treated as a circular annulus at each location, giving  $D = 2(r_{c,o}^{(i)} - r_{c,i}^{(i)})$  where  $r_{c,o}^{(i)}$  is the cooling channel outer radius and  $r_{c,i}^{(i)}$  is the inner radius. In the expression  $f$  is the friction loss coefficient and is set equal to 0.03 as it typically ranges from 0.02-0.05. The coolant flow is treated as incompressible and the density  $\rho$  is taken to be  $260 \text{ kg/m}^3$ , corresponding to supercritical cryogenic methane at elevated pressure. The local flow velocity is then computed from mass continuity, similar to Equation 18.

## 3.5 Heat Transfer Model

The resistance method is used to formulate a heat transfer model. Axial conduction is neglected and only radial outward heat flow is considered. The resistance method is developed from an analogy between the flow of electrical current in circuits and the flow of heat in materials and Ohm's law which states  $\Delta V = IR$ . Electrical current  $I$  is analogous to the heat rate  $\dot{q}$ , and difference in electric potential (voltage)  $\Delta V$  is analogous to difference in temperature  $\Delta T$ . This analogy only holds for one-dimensional heat flow and can be more clearly seen by considering Fourier's law of conduction in 1D as shown in Equation 26, where  $\kappa$  is the material thermal conductivity. The last expression corresponds directly to a rearrangement of Ohm's law as  $I = \Delta V / R$ . Thus the thermal resistance for 1D conduction is  $R_{t,cond} = \Delta x / (\kappa A)$ .

$$\dot{q} = -\kappa A \nabla T \approx -\kappa A \frac{\Delta T}{\Delta x} = \frac{\kappa A}{\Delta x} (T_{low} - T_{high}) = \frac{(T_{low} - T_{high})}{R_{t,cond}} \quad (26)$$

An equivalent expression for radial conduction is shown in Equation 27, and for radial convection in Equation 28 where  $h$  is the convection coefficient typically found from a correlation.

$$R_{t,cond} = \frac{\ln(r_2/r_1)}{2\pi\kappa\Delta z} \quad (27)$$

$$R_{t,conv} = \frac{1}{h2\pi r\Delta z} \quad (28)$$

A thermal circuit may be drawn and thermal resistances combined in the same way as electrical resistances. At each axial location a thermal circuit such as that shown in Figure 2 is constructed. This diagram is meant to be illustrative only, in the model the inner wall is discretized into a specified number of radial nodes rather than just placing nodes on the bounding surfaces.

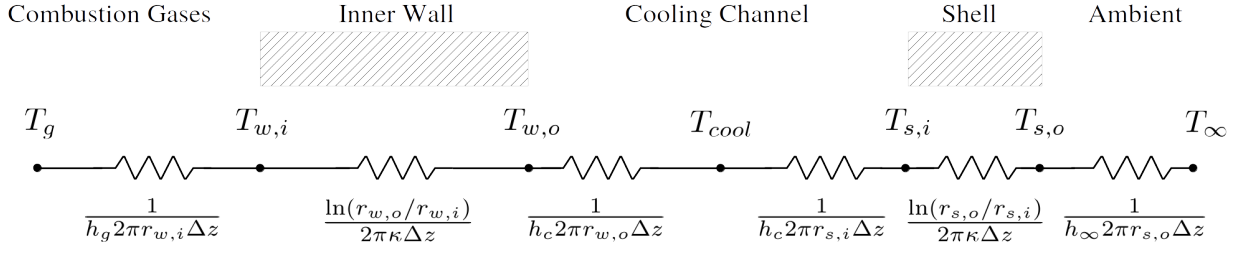


Figure 2: Example thermal circuit accounting for outward radial heat flow. Such a circuit is constructed at each axial location in the engine.

The temperatures  $T_g$  and  $T_{\infty}$  are known, so the heat rate may be computed as shown in Equation 29 for each axial location  $i$ .

$$\dot{q}^{(i)} = \frac{T_g^{(i)} - T_{\infty}}{\sum R_t^{(i)}} \quad (29)$$

Next a control volume is drawn around the cooling channel node as shown in Figure 3 and an energy rate balance performed. This shows that the total radial heat flow either goes into raising the temperature of the coolant or is transferred to the environment.

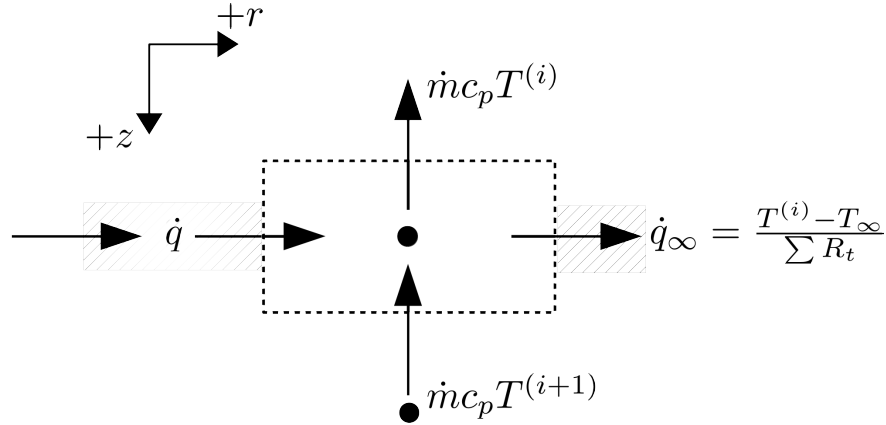


Figure 3: Energy balance drawn around a node in the cooling channel.

The coolant temperature at the jacket inlet (nozzle exit) is specified at a known cryogenic condition, with  $T = 90K$ . The temperature of the coolant is computed successively at each axial location, starting at the nozzle exit and walking upstream. The energy balance at axial node  $i$  is written as shown in Equation 30, where  $\sum R_t$  is the sum of the thermal resistances between the cooling channel and the ambient temperature,  $T_{cool}^{(i+1)}$  is known (axially downstream node), and  $c_p$  is the specific heat capacity of the coolant. This is rearranged to solve for  $T_{cool}^{(i)}$  as shown in Equation 31.

$$\dot{q}^{(i)} = \dot{m}_{cool} c_p (T_{cool}^{(i)} - T_{cool}^{(i+1)}) + \frac{T_{cool}^{(i)} - T_{\infty}}{\sum R_t^{(i)}} \quad (30)$$

$$T_{cool}^{(i)} = \frac{\dot{q}^{(i)} + \dot{m}_{cool} c_p T_{cool}^{(i+1)} + (T_{\infty} / \sum R_t^{(i)})}{\dot{m}_{cool} c_p + (1 / \sum R_t^{(i)})} \quad (31)$$

Once the temperature of the coolant is known at each axial location the rest of the temperatures may be readily computed by analogy with Ohm's law, as represented in Equation 32 where  $\Delta T$  is relative to a known temperature and  $R_t$  is the total thermal resistance between the nodes in consideration. Care must be taken

to use the appropriate sign and heat rate.

$$\Delta V = IR \rightarrow \Delta T = \dot{q}R_t \quad (32)$$

The total rate of thermal energy absorbed by the coolant may then be computed as shown in Equation 33.

$$\dot{q}_{cool,tot} = \dot{m}_{cool}c_p(T_{outlet} - T_{inlet}) \quad (33)$$

The Nusselt number is computed using the Gnielinski correlation and is used to find the convective heat transfer coefficient, as shown in Equation 34, with the friction factor  $f$  computed from Equation 35.

$$Nu_d = \frac{(f/8)(Re - 1000)Pr}{(1 + 12.7(f/8)^{1/2}(Pr^{2/3} - 1))} = \frac{hD}{\kappa_{fluid}} \quad (34)$$

$$f = (0.79 \ln(Re) - 1.64)^{-2} \quad (35)$$

The Reynolds numbers are computed using the hydraulic diameter as the length scale. The Prandtl number is a dimensionless number quantifying the ratio of momentum to thermal diffusivity as shown in Equation 36.

$$Pr = \frac{\nu}{\alpha} = \frac{c_p \mu}{\kappa} \quad (36)$$

The Prandtl number of the combustion gases is computed using Cantera and is set to 0.86 for the coolant methane.

### 3.6 Mechanical Stress Model

Only the mechanical stresses in the inner wall are computed. It is assumed that the rocket thrust is carried by the injector face so the chamber/nozzle are only responsible for carrying pressure and thermal expansion loads. The difference in pressure between the combustion gases in the engine and the fluid in the cooling jacket gives rise to compressive stresses in the inner wall since the cooling jacket is at higher pressure than the engine. A thin wall pressure vessel assumption is made and is used to find an expression for the circumferential (hoop) stress resulting from this pressure difference. The hoop stress is known to dominate over the axial (meridional) stress by a factor of 2, so the axial stress is not considered. The formula for hoop stress in a cone frustum is given by Equation 37, where  $\beta$  is the cone half angle. This formula is valid for the cylindrical combustion chamber sections as well with  $\beta = 0$ . The hoop stress is treated as uniform compressive (negative in sign) across the inner wall cross section. This expression is applied at each axial location.

$$\sigma_{hoop} = \frac{\Delta pr}{t \cos(\beta)} = \frac{(p_{gas} - p_{cool})r_{w,mean}}{t_w \cos(\beta)} \quad (37)$$

Circumferential stresses due to thermal expansion, arising from differences in temperature across the inner wall, are also present as given by Equation 38 [Sutton and Biblarz, 2010]. In this equation  $\lambda$  is the coefficient of thermal expansion,  $E$  is Young's Modulus, and  $\nu$  is Poisson's ratio. The thermal stresses are compressive on the inner wall surface (negative sign) and vary linearly through the thickness of the inner wall to a tensile value equal in magnitude on the inner wall outer surface.

$$\sigma_{therm} = 2\lambda E \Delta T / (1 - \nu) = 2\lambda E (T_{w,o} - T_{w,i}) / (1 - \nu) \quad (38)$$

The thermal and hoop stresses add linearly, indicating that the peak mechanical stress occurs at the inner wall inner surface and are equal to  $\sigma_{hoop} + \sigma_{therm}$ .

### 3.7 Performance Calculations

Once the flow model is solved performance metrics may be computed. The ideal thrust and  $I_{sp}$  are computed as shown in Equations 39 and 40.

$$F_{ideal} = \dot{m}u_e + (p_e - p_\infty)A_e \quad (39)$$

$$I_{sp,ideal} = F_{ideal} / (\dot{m}g_0) \quad (40)$$



These expressions assume that the gas velocity is perfectly axial at the nozzle exit which is a reasonable assumption for a bell contoured nozzle. However, since this analysis uses a conical nozzle the ideal momentum thrust (first term in thrust equation) is augmented by a correction factor accounting for flow divergence given by Equation 41. The actual thrust and  $I_{sp}$  are then computed as shown in Equations 42 and 43, where  $g_0$  is the sea level acceleration due to gravity.

$$\alpha = 0.5(1 + \cos(\beta_{nd})) \quad (41)$$

$$F = \alpha \dot{m} u_e + (p_e - p_\infty) A_e \quad (42)$$

$$I_{sp} = F / (\dot{m} g_0) \quad (43)$$

$I_{sp}$  is a measure of efficiency and may be thought of as the thrust per unit weight from rate propellant and has units of seconds.

## 4 Material Properties, and Thermal Boundary Conditions

The engine structure is constructed of steel with material properties given in Table 2.

Table 2: Mechanical properties used in the model, based on steel.

| Symbol     | Property                         | Value            |
|------------|----------------------------------|------------------|
| $\kappa$   | thermal conductivity             | 45 $W/m \cdot K$ |
| $E$        | Young's Modulus                  | 200GPa           |
| $\nu$      | Poisson's ratio                  | 0.29             |
| $\lambda$  | coefficient of thermal expansion | 11e-06 $m/(mK)$  |
| $\sigma_y$ | Yield stress                     | 350Mpa           |
| $\rho$     | Density                          | 8000 $kg/m^3$    |

Other properties related to thermal boundary conditions and supercritical methane (for the cooling loop) are given in Table 3.

Table 3: Thermal boundary conditions and Methane properties.

| Symbol         | Property                                   | Value                |
|----------------|--|----------------------|
| $T_{reac}$     | Reactant temperature pre-combustion        | 200 $K$              |
| $p_\infty$     | Ambient pressure                           | 0.1 atm              |
| $T_\infty$     | Ambient temperature                        | 200K                 |
| $h_\infty$     | Convection coefficient to ambient          | 10 $W/m^2 K$         |
| $\rho_{CH4}$   | Supercritical methane density              | 260 $kg/m^3$         |
| $\kappa_{CH4}$ | Supercritical methane thermal conductivity | 40e-03 $W/m \cdot K$ |
| $Pr_{CH4}$     | Supercritical methane Prandtl number       | 0.86                 |
| $\mu_{CH4}$    | Supercritical methane dynamic viscosity    | 15e-06 $Pa \cdot s$  |
| $T_{CH4,cool}$ | Cooling jacket inlet temperature           | 90K                  |

## 5 Design Structure Matrix

As implemented the graph representing the model is acyclic and thus each component may be solved successively without iteration. A simplified design structure matrix is as shown in Figure 4.

| Component              |    | 1 | 2 | 3 | 4 | 5 | 6 | 7 | 8 | 9 | 10 | 11 | 12 |
|------------------------|----|---|---|---|---|---|---|---|---|---|----|----|----|
| Thermochemical Solver  | 1  |   | x |   | x | x | x |   |   |   |    |    |    |
| Geometry Generator     | 2  |   |   | x | x | x | x |   | x |   |    |    |    |
| Mesher                 | 3  |   |   |   | x | x |   | x |   |   |    |    |    |
| Flow Model             | 4  |   |   |   |   | x | x | x |   |   |    |    |    |
| Heat Transfer          | 5  |   |   |   |   |   |   | x |   |   |    |    | x  |
| Performance            | 6  |   |   |   |   |   |   |   |   | x | x  |    |    |
| Stress Model           | 7  |   |   |   |   |   |   |   |   |   |    | x  |    |
| Mass                   | 8  |   |   |   |   |   |   |   |   |   |    |    |    |
| Thrust Constraint      | 9  |   |   |   |   |   |   |   |   |   |    |    |    |
| Isp Constraint         | 10 |   |   |   |   |   |   |   |   |   |    |    |    |
| Stress Constraint      | 11 |   |   |   |   |   |   |   |   |   |    |    |    |
| Temperature Constraint | 12 |   |   |   |   |   |   |   |   |   |    |    |    |

Figure 4: Design structure matrix with no iterative dependencies.

In reality there is cyclic coupling between the heat transfer model and the flow model. As mentioned previously this coupling is weak which is why it was not pursued for the simplified model here. Additionally there is coupling between the heat transfer model and the thermochemical solver. The coolant stream mixes with the main fuel flow and raises its temperature, augmenting the heat release and post combustion state. This effect is ignored in the current model implementation. Additionally there is coupling between the stress model and the flow model as components under stress undergo displacement, altering the engine cross section slightly. This would impact the flow but again, this is likely to be a weak coupling.

## 6 Optimization Results

The intention for this project was to perform initial optimization studies using `scipy.optimize` and to transition to use of OpenMDAO. However, due to time constraints, only preliminary studies using `scipy.optimize` are presented here. All results shown utilize the SLSQP optimization algorithm. This optimizer was selected as it is easy to interface with as it accepts both bounds and constraints and utilizes gradient information. Other gradient based algorithms provided in `scipy.optimize`, such as BFGS and L-BFGS-B, accept either one or the other, or neither. Working with bounds and constraints allows for simple objective function specification, without the complication of introducing a penalty term. All design variables are scaled from 0-1 and physical limits are provided. Jacobian computation is left up to the optimizer using finite differences with the default settings.

### 6.1 Unconstrained Optimization

As a first test all constraints are removed. The expected behavior in this situation is for the optimizer to reduce the chamber radius and length to their minimal values, to increase the nozzle angles  $\beta_{nc}$  and  $\beta_{nd}$  to their maximal limits, to decrease the nozzle expansion ratio to its minimal value, and to decrease the inner wall thickness to its minimal value. The initial design point provided to the optimizer is  $x_i = 0.5$  for all normalized design variables. The optimizer converged quickly, in just 2 iterations requiring 26 function evaluations and 2 Jacobian evaluations. Table 4 shows that the optimal values mentioned above are exactly as expected.

Table 4: Design variable limits and optimal values for unconstrained optimization.

| Design Var.      | Limits          | Optimal Value |
|------------------|-----------------|---------------|
| $r_c$            | (0.1, 0.5)      | 0.1           |
| $L_c$            | (0.1, 0.4)      | 0.1           |
| $\beta_{nc}$     | (30, 60)        | 60            |
| $\beta_{nd}$     | (15, 25)        | 25            |
| $\epsilon$       | (2, 30)         | 2             |
| $t_w$            | (0.005, 0.05)   | 0.005         |
| $t_j$            | (0.001, 0.05)   | 0.0255        |
| $t_s$            | (0.001, 0.0015) | 0.00125       |
| $\dot{m}_f$      | (10, 11)        | 11            |
| $\phi$           | (0.8, 1.2)      | 1.2           |
| $p_c$            | (5, 40)         | 40            |
| $f_c$            | (0.01, 0.5)     | 0.255         |
| Objective (mass) | -               | 4.7           |

## 6.2 Isp-only Constraint

Next an  $I_{sp}$  constraint is added and the design variable limits are left unchanged. First, a minimal limit of 300s is imposed. The optimizer converges under these settings in 9 iterations, requiring 119 objective calls and 9 Jacobian evaluations, with the optimal design point shown in Table 5. Most of the design variables are the same as the unconstrained case and are not included in the table. The nozzle expansion ratio  $\epsilon$  has increased from 2 to 5.7 and the diverging nozzle angle has decreased to 22.6 deg to satisfy the  $I_{sp}$  constraint, resulting in a mass increase from 4.7 to 12.7 kg. Similar behavior is seen when the  $I_{sp}$  constraint is increased further to 325s, where the nozzle expansion ratio is increased until the constraint is met. Under these limits the mass increases to 44.6 kg.

Table 5: Design variable limits and optimal values for unconstrained optimization.

| Design Var. / Other | Limits   | $I_{sp} = 300 \text{ s}$ | $I_{sp} = 325 \text{ s}$ |
|---------------------|----------|--------------------------|--------------------------|
| $\beta_{nd}$        | (15, 25) | 22.6                     | 25                       |
| $\epsilon$          | (2, 30)  | 5.7                      | 23.6                     |
| Objective (mass)    | -        | 12.7                     | 44.6                     |
| Iterations          | -        | 9                        | 22                       |
| Function Calls      | -        | 119                      | 279                      |

The  $I_{sp}$  constraint was increased to 350s and under these limits the optimization fails with warning message 'Positive directional derivative for linesearch.' This is not surprising as the chamber pressure and mass flow rate cannot be further increased due to the limits, both of which lead most directly to an increase in  $I_{sp}$ . Further explorations are not conducted here as specifying only engine  $I_{sp}$  is not a realistic design scenario for chemical propulsion.

## 6.3 Thrust-only Constraint

Next the optimization was explored using a minimum thrust constraint. During these explorations a deficiency in the model was discovered. For some designs, the throat area computed using Equation 4 would be larger than the chamber area, leading to a negative converging section length via Equation 6. This leads to garbage output which would sometimes satisfy the constraints but would not be physically meaningful or consistent. When this was observed, the minimal chamber radius  $r_c$  was increased along with the maximal chamber pressure  $p_c$ . It would be possible to estimate the largest throat area required given the bounds on the chamber pressure, mass flow rate, and estimated (or computed) gas properties, and then set the lower

limit of the chamber radius as some factor larger than this. However this approach may be overly prohibitive as it is not guaranteed that the optimizer will explore areas of the design space which have this issue.

The minimal combustion chamber radius and maximal pressure were both increased and the thrust constraint varied from 200kN to 400kN with the resulting optimal designs shown in Table 6. The rows with bold entries highlight the design variables which change in response to the constraint, which are namely the fuel mass flow rate and equivalence ratio. Increasing either of these variables increases the overall mass flow rate through the engine which is directly proportional to the total thrust as seen in the momentum thrust term of Equation 42. The mass of the engine increases with increasing thrust constraint due to the coupling between the throat area and mass flow rate in Equation 4. In that expression there are competing effects of increasing throat area proportionally to the total mass flow rate and decreasing throat area with increasing chamber pressure. The optimizer appears to see a steep direction of descent towards increasing pressure as all optimal designs but up against the prescribed limit.

Table 6: Design variable limits and optimal designs for varying minimum thrust constraint.

| Design Var. / Other | Limits     | $F = 200\text{kN}$ | $F = 250\text{kN}$ | $F = 300\text{kN}$ | $F = 400\text{kN}$ |
|---------------------|------------|--------------------|--------------------|--------------------|--------------------|
| $r_c$               | (0.3, 0.8) | 0.3                | 0.3                | 0.3                | 0.3                |
| $L_c$               | (0.3, 0.4) | 0.3                | 0.3                | 0.3                | 0.3                |
| $\beta_{nc}$        | (30, 60)   | 60                 | 60                 | 59                 | 60                 |
| $\beta_{nd}$        | (5, 25)    | 25                 | 25                 | 25                 | 20.9               |
| $\epsilon$          | (10, 40)   | 10                 | 10                 | 10                 | 10.2               |
| $\dot{m}_f$         | (2, 30)    | <b>14.2</b>        | <b>18.8</b>        | <b>21.4</b>        | <b>30</b>          |
| $\phi$              | (0.8, 1.2) | <b>1.07</b>        | <b>1.17</b>        | <b>1.08</b>        | <b>1.2</b>         |
| $p_c$               | (5, 80)    | 80                 | 80                 | 80                 | 80                 |
| $I_{sp}$            | -          | 303.8              | 308.6              | 304.1              | 314.3              |
| Objective (mass)    | -          | <b>40.8</b>        | <b>43.6</b>        | <b>46.4</b>        | <b>57.4</b>        |
| Iterations          | -          | 4                  | 4                  | 4                  | 9                  |
| Function Calls      | -          | 52                 | 53                 | 52                 | 105                |

To better understand how the engine characteristics change with the thrust constraint, a variety of quantities are plotted against the engine axis for each thrust level in Figure 5. The top row of the figure shows the combustion gas temperature, flow speed, and heat flux through the inner surface of the inner wall. From these plots it is clear that the engine length increases with increasing thrust, consistent with the increased throat area and similar expansion ratios and angles. The first two plots show that the flow state variables do not change greatly as the thrust is increased. The trends seen in the heat flux plot seem counter intuitive at first glance, as the peak heat flux is largest for the engine with the smallest thrust. This trend actually makes sense as the engine with the least thrust has the smallest throat and heat flux is the heat rate per unit area. Thus a smaller area with a similar overall heat rate leads to a larger heat flux. The heat flux peaks at the throat for each engine, with the smallest engine having its throat farthest downstream due to the same nozzle converging section angle.

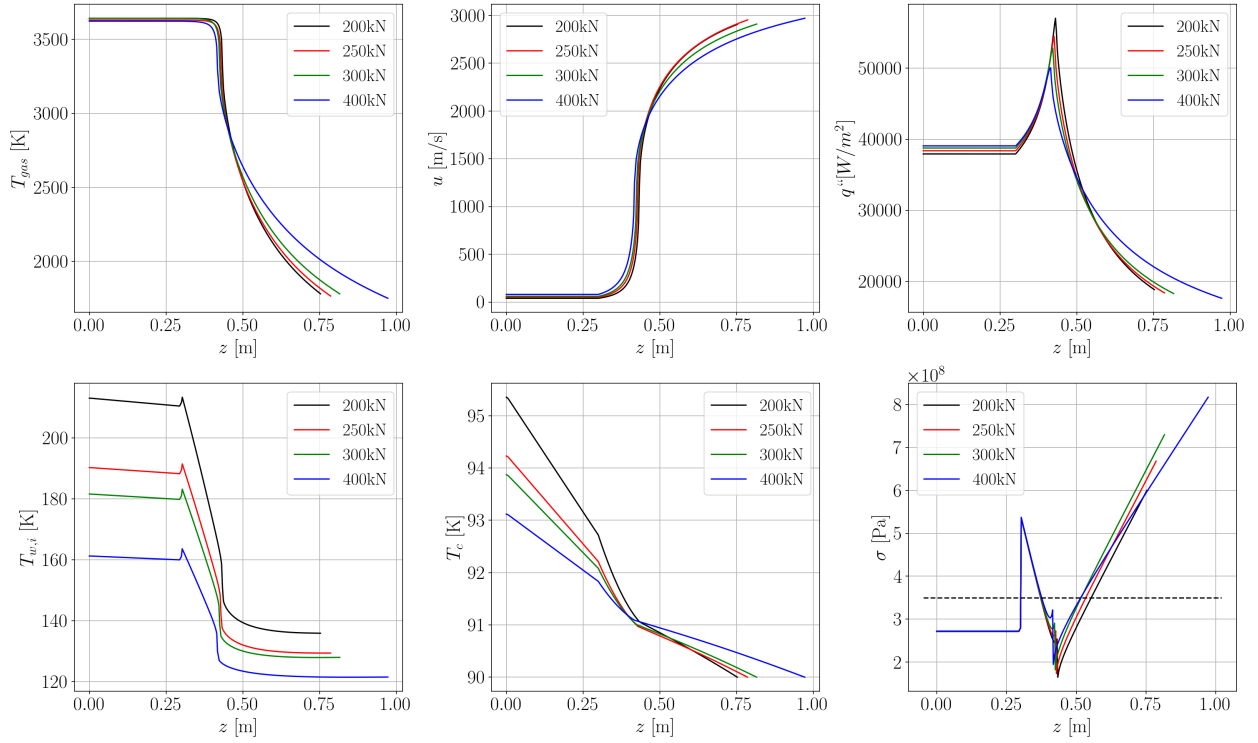


Figure 5: Comparison of optimal solutions for varying thrust constraints. Top row: Gas temperature, gas velocity, and heat flux through the inner wall. Bottom row: Inner wall inside surface temperature, coolant temperature, and mechanical stress.

The bottom row of Figure 5 shows the inner wall surface temperature, the coolant temperature, and the mechanical stress where the black dashed line is the yield strength. The trends in the temperature profiles are consistent with the earlier observations regarding the heat flux. This is especially evident when observing the slope of the coolant temperature profiles just upstream of the throat. The smallest engine has the highest heat flux at the throat and the steepest temperature increase. There is not a huge variation among the designs in terms of mechanical stress. The plot shows that none of the engines satisfy the stress constraint, which none are subject to.

## 6.4 Thrust and Isp Constraints

Here both thrust and  $I_{sp}$  constraints are included. The maximum allowable chamber pressure was also increased to allow for higher  $I_{sp}$  values to be obtained. For all cases shown here the thrust constraint is set to 300kN and the  $I_{sp}$  constraint is varied from 325-350s, and for direct comparison another design is optimized with only the thrust constraint including the higher chamber pressure. This range of  $I_{sp}$  was selected due to the values reported in Table 6, which vary non-monotonically with thrust constraint between 303 and 314s. The results of the optimization with both constraints are summarized in Table 7, where the rows for  $r_c$ ,  $L_c$ , and  $\beta_{nc}$  are deleted since the limits are the same as for Table 6, and all designs take the same values of 0.3m, 0.3m, and 60deg respectively.

As the  $I_{sp}$  constraint is increased, the nozzle area ratio  $\epsilon$  increases dramatically from 10 to 40, hitting the limits on either end. Opposing this is a decrease in fuel mass flow rate. Both of these trends makes sense as  $I_{sp} = F/(\dot{m}g_0)$ . To increase the  $I_{sp}$  the mass flow rate is decreased, but to maintain the thrust the expansion ratio is increased, as further expansion means greater gas acceleration and thrust. This can be seen clearly in the top-middle plot for velocity in Figure 6, where the exit plane exhaust velocities are ordered by  $I_{sp}$ . However the larger expansion ratios lead to much longer and thus heavier engines, with the engine mass doubling between the no  $I_{sp}$  constraint case and that with an  $I_{sp}$  of 350s.

Table 7: Design variable limits and optimal designs for minimum thrust constraint of 300kN and varying  $I_{sp}$  constraint. Note that the solution for  $I_{sp} = 350$  is not converged: the optimizer exited with a warning message regarding no descent direction in line search, although the design is feasible.

| Design Var. / Other | Limits     | No Isp. const. | $I_{sp} = 325s$ | $I_{sp} = 340s$ | $I_{sp} = 350s^{**}$ |
|---------------------|------------|----------------|-----------------|-----------------|----------------------|
| $\beta_{nd}$        | (5, 25)    | 25             | 25              | 25              | 21.9                 |
| $\epsilon$          | (10, 40)   | <b>10</b>      | <b>25.5</b>     | <b>34</b>       | <b>40</b>            |
| $\dot{m}_f$         | (2, 40)    | <b>20.2</b>    | <b>18.5</b>     | <b>17.5</b>     | <b>16.9</b>          |
| $\phi$              | (0.8, 1.2) | 0.99           | 0.97            | 0.96            | 0.96                 |
| $p_c$               | (5, 100)   | 100            | 100             | 100             | 100                  |
| $I_{sp}$            | -          | 301            | 325             | 340             | 350                  |
| Objective (mass)    | -          | <b>43.0</b>    | <b>63.6</b>     | <b>74.4</b>     | <b>88.7</b>          |
| Iterations          | -          | 4              | 5               | 5               | 9                    |
| Function Calls      | -          | 53             | 65              | 66              | 65                   |

The trends in the top row of Figure 6 show that the flow properties and heat fluxes do not vary greatly between designs, other than the effects of a longer engine. However the trends for inner wall and coolant temperatures are opposite of that seen for increasing thrust: engines with smaller  $I_{sp}$  have lower temperatures, whereas engines with lower thrust have higher temperatures, as seen in the last section. This is mostly an effect of increasing engine length as a result of the increased expansion ratio. As before all engines violate the stress constraint.

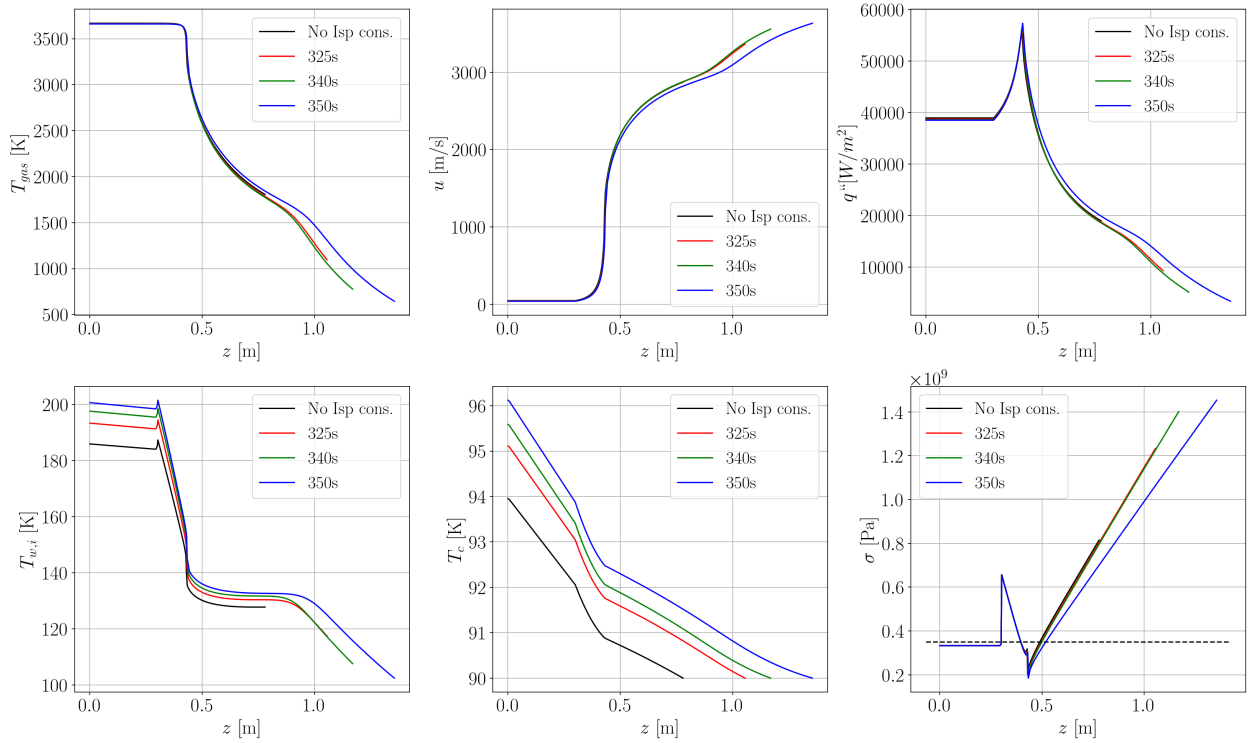


Figure 6: Comparison of optimal solutions for varying  $I_{sp}$  constraints with a minimal thrust constraint of 300kN. Top row: Gas temperature, gas velocity, and heat flux through the inner wall. Bottom row: Inner wall inside surface temperature, coolant temperature, and mechanical stress.

## 6.5 Thrust, Isp, and Stress Constraints

Next the stress constraint is included in addition to a minimal thrust of 300kN and an  $I_{sp}$  of 325s, with a comparison being made between the cases with and without the constraint as shown in Table 8. The design including the stress constraint is not converged as the optimizer exited with a warning though the solution is still feasible as all constraints are met. Introducing the stress constraint leads to alteration of geometric design variables which previously had not been altered. In all previous results the wall thickness  $t_w$  was pegged to its lower limit 5mm, while here it takes a value of 17.2mm. Additionally the cooling jacket thickness  $t_j$  has increased to its maximal value. This has occurred in conjunction with a drastic decrease in the coolant fraction  $f_c$ . Both of these trends make sense, as they seek to reduce the pressure in the cooling jacket and thus the stress in the inner wall. Interestingly both optimal designs select the same pressure, fuel mass flow rate, and equivalence ratio, but with different nozzle expansion ratios and angles. The design with the stress constraint has a much greater mass than the design without due to the increased wall thickness and shallower expansion angle.

Table 8: Comparison of optimal designs with minimal thrust of 300kN,  $I_{sp}$  of 325, with and without the stress constraint.

| Design Var.      | Limits          | No stress. cons. | With stress cons.** |
|------------------|-----------------|------------------|---------------------|
| $\beta_{nd}$     | (5, 25)         | 25               | 21.3                |
| $\epsilon$       | (10, 40)        | 25.2             | 23.2                |
| $t_w$            | (0.005, 0.05)   | <b>0.005</b>     | <b>0.0172</b>       |
| $t_j$            | (0.001, 0.05)   | <b>0.0255</b>    | <b>0.05</b>         |
| $t_s$            | (0.001, 0.0015) | 0.00125          | 0.001               |
| $\dot{m}_f$      | (2, 40)         | 18.5             | 18.5                |
| $\phi$           | (0.8, 1.2)      | 0.97             | 0.97                |
| $p_c$            | (5, 100)        | 100              | 100                 |
| $f_c$            | (0.01, 0.5)     | <b>0.255</b>     | <b>0.01</b>         |
| Objective (mass) | -               | <b>63.6</b>      | <b>236.9</b>        |
| Iterations       | -               | 5                | 23                  |
| Function Calls   | -               | 65               | 282                 |

Figure 7 compares the flow state, heat transfer/temperature effects, and stress. The gas temperature and velocity are similar between the two cases which makes sense since the thermochemical design variables are the same although the nozzle shapes are different. There is a dramatic difference between the stress constrained and non-stress constrained cases in terms of heat fluxes and wall temperatures. The inner wall and coolant temperatures of the stress constrained engine are much greater, especially the inner wall temperature which is more than 1000K higher. The decreased heat flux and increased temperature make sense as a thicker wall presents a greater resistance to heat flow. A greater resistance leads to less heat flow, and less heat flow implies less temperature difference between the entities exchanging heat. The bottom right plot of the stress shows that indeed the stress constraint is satisfied, with the stress curve lying below the yield stress.

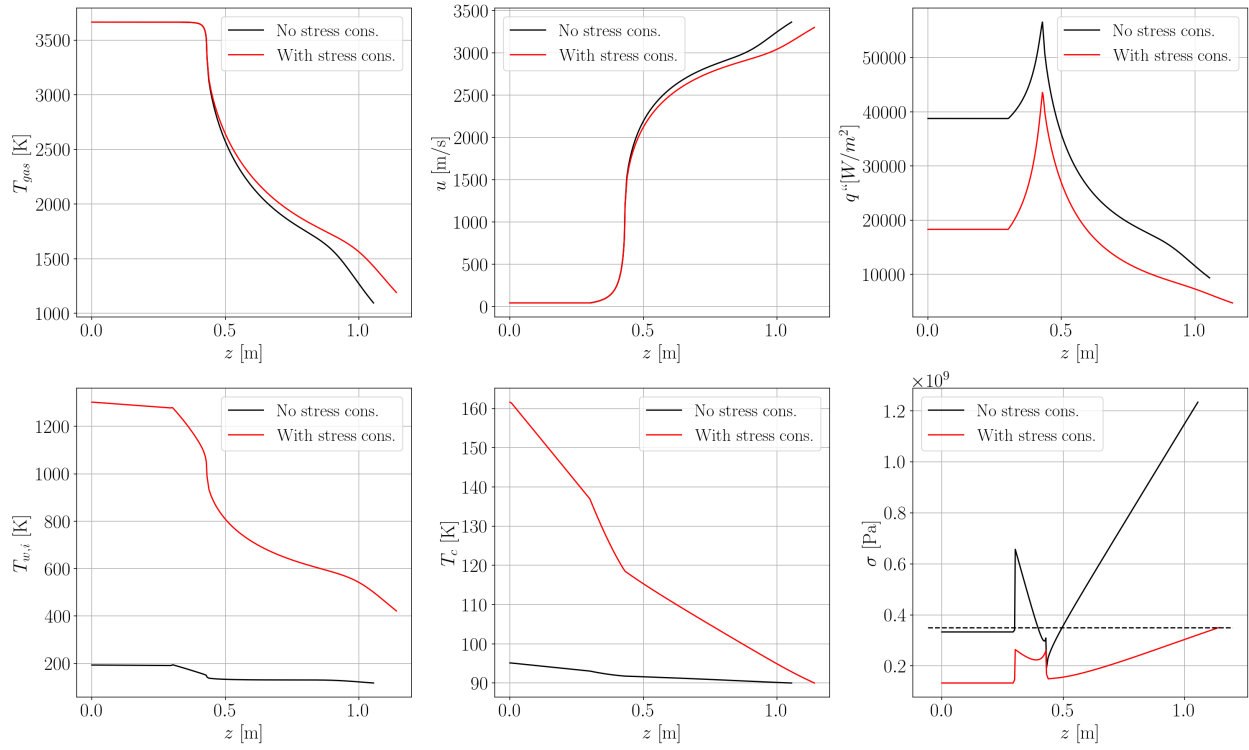


Figure 7: Comparison of optimal solutions for a thrust constraint of 300kN, Isp constraint of 325s, with and without the mechanical stress constraint. Top row: Gas temperature, gas velocity, and heat flux through the inner wall. Bottom row: Inner wall inside surface temperature, coolant temperature, and mechanical stress.

Figure 8 shows the inner wall temperatures across its full thickness instead of just on the surface, as well as the components which contribute to the overall stress, with the non-stress constrained case shown on the left and the constrained case on the right. In the non stress constrained case the pressure induced hoop stress dominates, while in the constrained case they are more balanced. The thermal stresses are larger than the pressure stresses only near the nozzle throat, while the pressure stresses grow large towards the nozzle exit where the coolant pressure is highest. It is interesting that a temperature constraint was not necessary until the stress constraint was introduced, showing that these are competing effects.



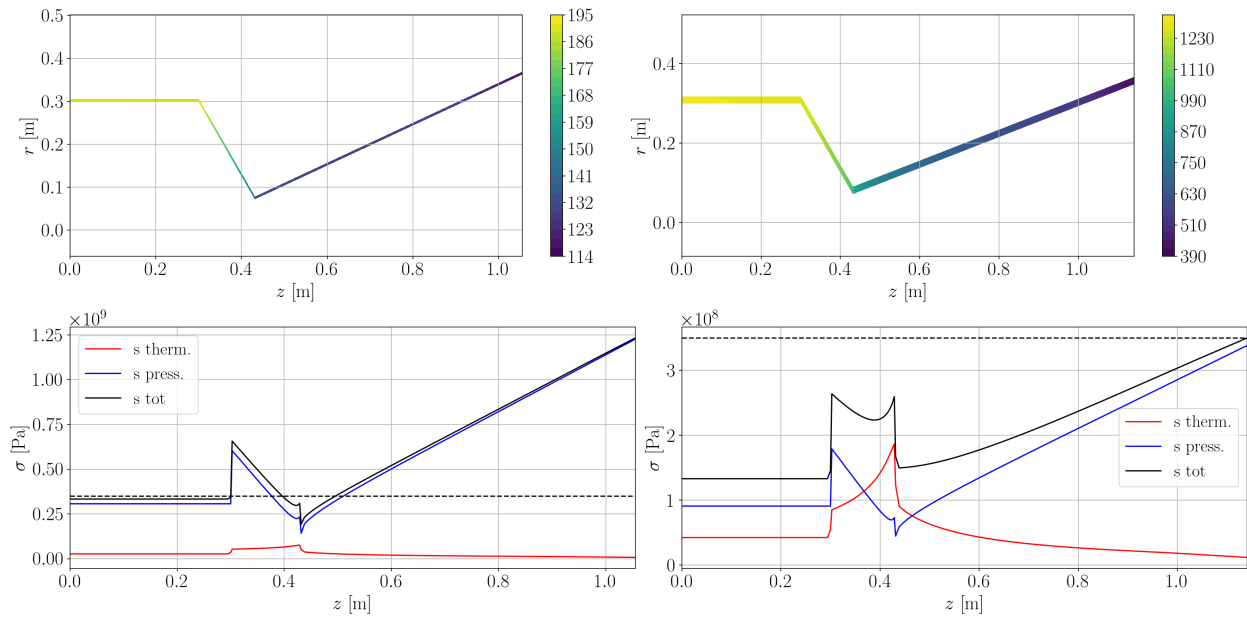


Figure 8: Comparison of optimal solutions for a thrust constraint of 300kN, Isp constraint of 325s, with and without the mechanical stress constraint. Top row: Gas temperature, gas velocity, and heat flux through the inner wall. Bottom row: Inner wall inside surface temperature, coolant temperature, and mechanical stress.

## 6.6 All constraints

A temperature constraint of  $T_{max} = 700K$  is introduced to complete all constraints given in the initial problem statement. Table 9 compares the results with and without the temperature constraint. The designs are remarkably similar to one another, with the only substantial difference being the cooling jacket thickness which is much smaller with the temperature constraint. The mass difference between the engines is very small, given that the designs are very similar.

Table 9: Comparison of optimal designs including all constraints as compared to the case without the temperature constraint.

| Design Var.      | Limits          | No temp. cons. | With temp cons. |
|------------------|-----------------|----------------|-----------------|
| $\beta_{nd}$     | (5, 25)         | 21.3           | 21.3            |
| $\epsilon$       | (10, 40)        | 23.2           | 23.2            |
| $t_w$            | (0.005, 0.05)   | <b>0.0172</b>  | <b>0.0176</b>   |
| $t_j$            | (0.001, 0.05)   | <b>0.05</b>    | <b>0.014</b>    |
| $t_s$            | (0.001, 0.0015) | 0.001          | 0.001           |
| $\dot{m}_f$      | (2, 40)         | 18.5           | 18.5            |
| $\phi$           | (0.8, 1.2)      | 0.97           | 0.97            |
| $p_c$            | (5, 100)        | 100            | 100             |
| $f_c$            | (0.01, 0.5)     | 0.01           | 0.01            |
| Objective (mass) | -               | <b>236.9</b>   | <b>242.7</b>    |
| Iterations       | -               | 23             | 23              |
| Function Calls   | -               | 282            | 256             |

Figure 9 again compares flow profiles and thermal quantities. Unsurprisingly the gas temperatures and velocities are nearly identical since the geometric design parameters defining the engine interior cross section vs axial location are themselves nearly identical. However, the temperature profiles in the wall and coolant channel are very different from another. It is interesting to see how a seemingly small change between the

engine designs leads to a drastic difference in the temperatures. As explored previously the heat fluxes are greater in the engine with the lower internal wall temperature. The stresses appear very similar to another as well.

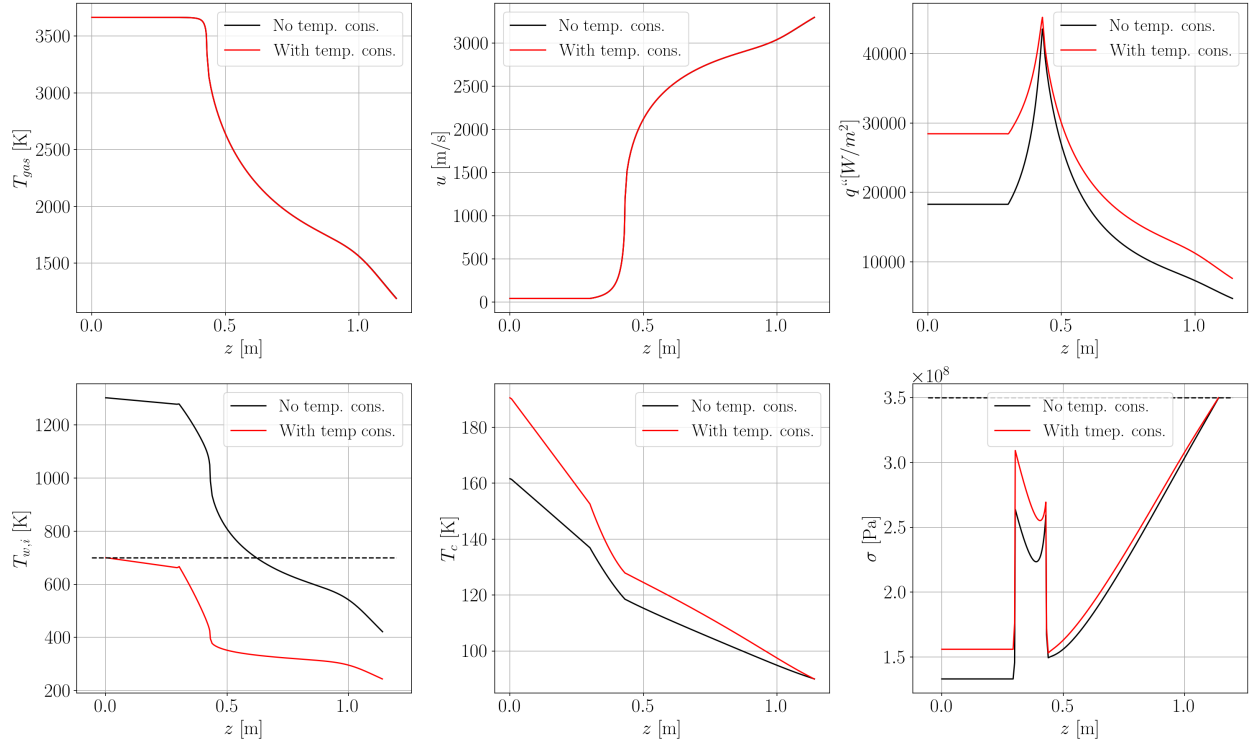


Figure 9: Comparison of optimal solutions for a thrust constraint of 300kN, Isp constraint of 325s, with and without the mechanical stress constraint. Top row: Gas temperature, gas velocity, and heat flux through the inner wall. Bottom row: Inner wall inside surface temperature, coolant temperature, and mechanical stress.

Figure 10 shows a more detailed comparison of the inner wall temperature profiles and the contribution to the overall state of stress from each component.

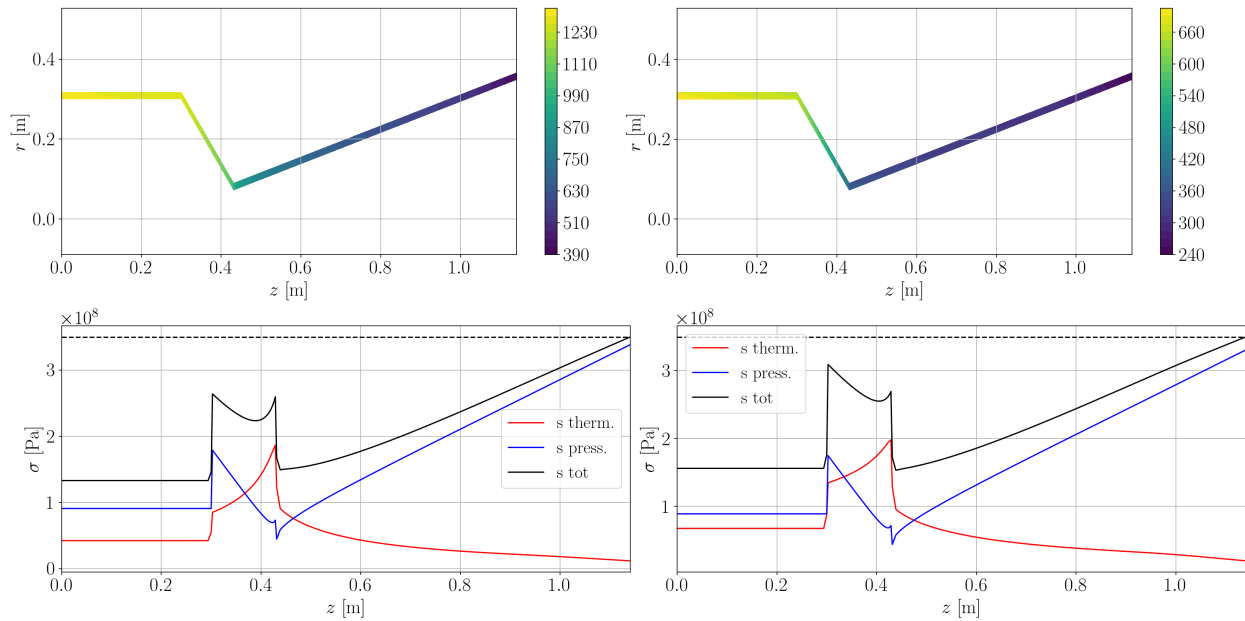


Figure 10: Comparison of optimal solutions for a thrust constraint of 300kN, Isp constraint of 325s, stress constraint, with and without the temperature constraint. Top row: Gas temperature, gas velocity, and heat flux through the inner wall. Bottom row: Inner wall inside surface temperature, coolant temperature, and mechanical stress.

## 7 Conclusions

A multidisciplinary analysis model of a rocket thrust chamber was devised and developed from scratch for this project. The model is simple and computationally efficient, running in just a few seconds, while still capturing many salient features of the engine performance. Preliminary optimization explorations were carried out using the SLSQP optimization algorithm as implemented in `scipy.optimize`. These explorations were performed around similar designs so that the effects of the various constraints could be examined. In general the engine mass tended to increase when the constraint were imposed, most notably once the stress constraint was brought to bear. This could have been expected since without the stress constraint the optimizer seeks to drive the thickness design variables toward their lower limit to decrease the mass, without consideration for strength. When increasing thrust constraints were imposed, the mass flow rate was increased to make up for the difference, since the chamber pressure was already at its maximal value. Applying an increasing  $I_{sp}$  constraint on top of a thrust requirement caused the mass flow rate to decrease and the nozzle expansion ratio to increase. Decreasing the mass flow rate decreases the momentum thrust while expanding the gas to a lower pressure in a larger nozzle accelerates the gas to higher velocity to make up this difference. When a stress constraint was also brought into the problem the engine mass increased greatly as did the temperatures. A temperature constraint on top of all this brought the temperatures back in line via minor modifications to the cooling channel geometry. A lot of work to understand the model and the optimization behavior is left to be done. The explorations here were around a small region of the possible design space. A valid criticism of this work is probably that there was too much effort spent in developing the model, leaving not enough time to really dive into the optimization process.

## References

- [Anderson, 2003] Anderson, J. D. (2003). *Modern Compressible Flow with Historical Perspective, Third Edition*. McGraw-Hill Higher Education, New York, NY.

- [Huzel and Huang, 1992] Huzel, D. K. and Huang, D. H. (1992). *Modern Engineering for Design of Liquid-Propellant Rocket Engines*. American Institute of Aeronautics and Astronautics, Washington DC.
- [Incropera et al., 2003] Incropera, F. P., Dewitt, D. P., Bergman, T. L., and Lavine, A. S. (2003). *Principles of Heat and Mass Transfer, Seventh Edition*. John Wiley and Sons Inc., Hoboken, New Jersey.
- [Sutton and Biblarz, 2010] Sutton, G. P. and Biblarz, O. (2010). *Rocket Propulsion Elements, Eighth Edition*. John Wiley and Sons, Hoboken, New Jersey.

## 8 Addendum

- Chamber radius should not be a design variable
- Use method of characteristics solver to trace out bell nozzle shape